UC Irvine
UC Irvine Previously Published Works

Title

Transcatheter Intraarterial Perfusion MRI Approaches to Differentiate Reversibly Electroporated Penumbra From Irreversibly Electroporated Zones in Rabbit Liver

Permalink

https://escholarship.org/uc/item/69g7r881

Journal

Academic Radiology, 27(12)

ISSN

1076-6332

Authors

Pan, Liang
Sun, Chong
Zhou, Kang
et al.

Publication Date

2020-12-01

DOI

10.1016/j.acra.2020.01.008

Peer reviewed

Transcatheter intraarterial perfusion MRI approaches to differentiate reversibly electroporated penumbra from irreversibly electroporated zones in rabbit liver

Liang Pan, MD[1,2,*], **Chong Sun, MD**[2,3,*], **Kang Zhou, MD**[2,4], **Matteo Figini, PhD**[2], **Bin Wang, MD**[2], **Junjie Shangguan, MS**[2], **Su Hu, MD**[2,5], **Jia Yang, MD**[2], **Wei Xing, MD**[1], **Jian Wang, MD**[2,6], **Yury Velichko, PhD**[2], **Vahid Yaghmai, MD**[2], **Zhuoli Zhang, MD**[2]

[1.]Department of Radiology, Third Affiliated Hospital of Soochow University, Changzhou, Jiangsu, China

[2.]Department of Radiology, Feinberg School of Medicine, Northwestern University, Chicago, IL, USA

[3.]Department of Orthopedics, Affiliated Hospital of Qingdao University, Qingdao, Shandong, China

[4.]Department of Radiology, Peking Union Medical College Hospital, Peking Union Medical College, Chinese Academy of Medical Sciences, Beijing, China

[5.]Department of Radiology, The First Affiliated Hospital of Soochow University, Suzhou, Jiangsu, China

[6.]Department of Radiology, Southwest Hospital, Third Military Medical University, Chongqing, China.

Abstract

Rationale and Objectives: To investigate whether transcatheter intraarterial perfusion (TRIP) magnetic resonance imaging (MRI) can differentiate reversible electroporation (RE) zones from irreversible electroporation (IRE) zones immediately after IRE procedure in the rabbit liver.

Materials and Methods: All studies were approved by the institutional animal care and use committee and performed in accordance with institutional guidelines. A total of thirteen healthy New Zealand White rabbits were used. After selective catheterization of the hepatic artery under X-ray fluoroscopy, we acquired TRIP-MRI at 20 minutes post-IRE using 3 mL of 5% intraarterial gadopentetate dimeglumine. Semi-quantitative (peak enhancement, PE; time to peak, TTP; wash-in slope, WIS; areas under the time-intensity curve, AUT, over 30, 60, 90, 120, 150, and 180 seconds after the initiation of enhancement) and quantitative (K^{trans}, v_e, and v_p) TRIP-MRI

Corresponding author: Zhuoli Zhang, Department of Radiology, Feinberg School of Medicine, Northwestern University, 737 N. Michigan Ave, 16th Floor, Chicago, IL 60611, USA Phone: 1-312-926-3874; Fax: 1-312-926-5991; zhuoli-zhang@northwestern.edu.
[*]Liang Pan and Chong Sun contributed equally.

parameters were calculated. The relationships between TRIP-MRI parameters and histological measurements and the differential ability of TRIP-MRI parameters was assessed.

Results: PE, AUT_{60}, AUT_{90}, AUT_{120}, AUT_{150}, AUT_{180}, K^{trans}, and v_e were significantly higher in RE zones than in IRE zones (all $P < 0.05$), and AUC for these parameters ranged from 0.91(95% CI, 0.80, 1.00) to 0.99 (95% CI, 0.98, 1.00). There was no significant difference in AUC between any two parameters (Z, 0–1.47; P, 0.14–1.00). Hepatocyte apoptosis strongly correlated with PE, AUT_{60}, AUT_{90}, AUT_{120}, AUT_{150}, AUT_{180}, K^{trans}, and v_p (the absolute value r, 0.6–0.7, all $P < 0.0001$).

Conclusion: AUT_{150} or AUT_{180} could be a potential imaging biomarker to differentiate RE from IRE zones, and TRIP-MRI permits to differentiate RE from IRE zones immediately after IRE procedure in the rabbit liver.

Introduction

Image guided ablation techniques are standard care for early stage liver cancer patients with surgically unresectable tumors or on waiting list for transplantation (1). However, thermal ablation techniques can damage healthy adjacent tissues due to a lack of clear margins between treated and untreated tissues, irreversible electroporation ablation can generate distinct margins between treated and untreated tissues by delivering electrical pulses to induce cell death through permanent cell membrane permeabilization (2), allowing improved targeted treatment of tumors while minimizing adverse effects. Irreversible electroporation (IRE) is a new non-thermal ablation technique with significant advantages over conventional thermal ablative approaches, such as preserving the integrity of blood vessels and bile ducts and not being affected by the local blood flow (3–6). Strong IRE pulses produce both a central ablation zone containing complete tissue necrosis (defined as irreversibly electroporated zone, IRE zone) and a surrounding zone containing viable tissue (defined as reversibly electroporated zone, RE zone) (7–9). These findings have been confirmed by histologic results (7–9). As RE zone remains viable, there is a risk of tumor recurrence or local tumor progression, which presents significant concerns for more widespread clinical application of this treatment (6).

Advanced MRI methods permit a more accurate prediction of IRE volumes and allow immediate assessment of tissue response for patient-specific optimization of the treatment protocol (7, 10, 11). However, previous studies focused only on correlating imaging findings and IRE histology to discriminate between tumor and normal tissue regions and not on predicting the margins of IRE and RE zones.

Transcatheter intraarterial perfusion (TRIP)-MRI is used clinically to measure local tumor perfusion by selective intraarterial (IA) catheter directed contrast agent injections (12, 13). Continuous iterative volumetric imaging over time of TRIP-MRI incorporates the benefits of

high spatial and temporal resolution with intraprocedural monitoring for objective perfusion quantification (14).

The purpose of our study was to investigate whether TRIP-MRI can differentiate RE zones from IRE zones immediately after the IRE procedure in the rabbit liver.

Materials and Methods

All experiments were approved by our institutional animal care and use committee and performed in accordance with National Institutes of Health guidelines.

Animal Model

Thirteen healthy New Zealand White rabbits (Covance, Denver, PA) were used. Basic anesthesia was induced by intramuscular injection of ketamine (100 mg/kg; Fort Dodge Animal Health, Fort Dodge, IA) and xylazine (5 mg/kg; Abbott Laboratories, North Chicago, IL). Rabbits were mechanically ventilated and maintained by inhalation of isoflurane (2–3% isoflurane with 100% oxygen, 3L/min) through a breathing mask during digital subtraction angiography (DSA), IRE, and MRI

Conventional DSA

Conventional DSA was performed using a C-arm unit (PowerMobil; Siemens Medical Solutions, Erlangen, Germany). The femoral artery access was obtained through surgical cutdown. A 2-F catheter (JB1; Cook Medical, Bloomington, IN) was advanced over a 0.018-inch diameter guidewire into hepatic arteries. DSA of hepatic arteries was performed using an iodinated contrast agent (iohexol, Omnipaque 350; Amersham, Princeton, NJ). All of the rabbit hepatic arteries were successfully catheterized with DSA.

IRE Procedures

The left median lobe of the liver was exposed after median laparotomy. Two paralleled MRI-compatible needle electrodes with 1-cm spacing (platinum-iridium materials; Microprobes, Gaithersburg, MD) were inserted into the center of the left median lobe with 1-cm depth. Next, the electrodes were connected to the IRE generator (ECM830; Harvard Apparatus, Holliston, MA) for application of 2000-V square wave pulses (number of pulses, 10; each pulse duration, 100 μs; the interval between pulses, 100 ms) to the targeted tissue (7, 15).

MR Imaging

MRI examinations were performed twenty minutes after IRE procedure using a 3T MRI scanner (MAGNETOM Skyra, Siemens Medical Solutions, Erlangen, Germany) with a 15-channel knee coil. Conventional MRI was performed before TRIP-MRI, and acquisition parameters are listed in Table 1. TRIP-MRI was repeatedly sampled for 250 times with 2.8 s sampling rate. 56 s after initiating TRIP-MRI, 3 ml of 5% gadopentetate dimeglumine (Magnevist; Bayer Schering Pharma, Whippany, NJ) was manually injected via the intra-arterial catheter over 6 s followed by a 3-ml saline flush at the same flow rate. Following TRIP-MRI, post-contrast T1-weighted (T1W) imaging was performed using the same sequence as pre-contrast T1W imaging.

Histologic Evaluation

Immediately after MRI, rabbits were euthanized by intravenous injection of Euthasol (200 mg/kg, Virbac AH Inc., Fort Worth, TX), and liver tissues were harvested. The sections, including the entire ablated zone (IRE and RE zone) and the surrounding normal liver tissue, were sampled along an orientation parallel to the electrode array. Liver samples were stained with hematoxylin-eosin (H&E) and terminal deoxynucleotidyl transferase dUTP nick end labeling (TUNEL) which was used as a marker of hepatocyte apoptosis. The RE and IRE zones were first identified on HE-stained slices. On the TUNEL-stained slices, hepatocyte apoptosis was quantified as the percentage of TUNEL-positive cells over the total number of cells in 10 random regions ($\times$ 200 magnification) on each slice.

Image Analysis

All the MRI images were analyzed by consensus of two radiologists using Jim software (version 7.0, Xinapse Systems, Essex, UK). Using post-contrast T1W images as reference (8, 11), three regions of interest (ROIs) were drawn within the hypo-intensity center (the IRE zone), the peripheral hyper-intensity region (the RE zone) on the axial section parallel to the electrode array, and in the normal liver parenchyma of the right lobe on TRIP-MRI images (7–9). A time-intensity curve (TIC) was generated for each ROI, and the semi-quantitative parameters were calculated: peak enhancement (PE, the maximal signal intensity minus baseline signal intensity), time to peak (TTP, the time difference between PE and the initiation of enhancement), wash-in slope (WIS, the maximal upslope reaching PE), and the areas under the TIC (AUT) over seconds (AUT_{30}, AUT_{60}, AUT_{90}, AUT_{120}, AUT_{150} and AUT_{180}) after the initiation of enhancement (16). Single-input extended Tofts model was used to perform quantitative measurements (17). The maps of the following parameters were generated: K^{trans}, the volume transfer constant from the plasma to the extra-vascular extra-cellular space (EES); v_e, the EES volume fraction; v_p, the blood plasma volume fraction (18). The mean values of each quantitative parameter (K^{trans}, v_e, and v_p) were measured in the same ROIs that were drawn for the TIC analysis.

Statistical Analysis

Statistical analysis was performed using SPSS (version 22.0; SPSS, Chicago, IL). The results are presented as mean ± standard deviation (SD). Differences in TRIP-MRI parameters and hepatocyte apoptosis among the normal liver parenchyma, the RE and IRE zones were determined by the Kruskal-Wallis test followed by pairwise comparisons. The diagnostic performance of TRIP-MRI parameters in differentiating RE from IRE zones was assessed by calculating the area under the receiver operating characteristic (ROC) curves (AUC), optimal cut-off values, sensitivity, specificity, positive and negative predictive values. The AUC for TRIP-MRI parameters were compared by Z test. The relationship between TRIP-MRI parameters and hepatocyte apoptosis was assessed by Pearson correlation coefficients (*r*). *P* < 0.05 was considered to indicate a significant difference in all statistical tests.

Results

MR Imaging

Representative MRI images of the liver after IRE procedure and the corresponding TICs derived from TRIP-MRI for the normal liver parenchyma, the RE and IRE zones were shown in Figure 1. The entire ablated regions were slightly hypo- or iso-intense on pre-contrast T1W images and hyper-intense on T2-weighted (T2W) images. On post-contrast T1W images, the entire ablated regions showed heterogeneous enhancement with the exception of a non-enhancing center and peripheral rim enhancement. The TICs and the maps of K^{trans}, v_e, and v_p clearly depicted heterogeneous perfusion of the entire ablated zone.

TRIP-MRI parameters for the normal liver parenchyma, the RE and IRE zones were listed in Table 2, Figure 2, and Figure 3. The results of the ROC curve analysis for TRIP-MRI parameters differentiating RE from IRE zones were summarized in Table 3. There was no significant difference in AUC between any two parameters (Z, 0–1.47; P, 0.14–1.00). AUT_{150} and AUT_{180} had the greatest ability to differentiate RE zone from IRE zone, with AUC of 0.99 (95% CI, 0.98, 1.00) for both, and an optimal cut-off value of 1066 for AUT_{150} and 1343 for AUT_{180}. Both AUT_{150} and AUT_{180} had 96% (25/26) accuracy, 100% (13/13) sensitivity, and 92% (12/13) specificity for all.

Histologic Findings

Representative H&E- and TUNEL-stained images of the normal IRE treated, and untreated liver parenchyma are shown in Figure 4.

On TUNEL-stained images, the average hepatocyte apoptosis (%) in the normal liver parenchyma, the RE zone, and IRE zone were 0.1 ± 0.08, 3.0 ± 1.3, and 23.4 ± 6.7, respectively. There were significant differences in hepatocyte apoptosis among the normal liver parenchyma, RE zone and IRE zone (RE vs IRE, $P = 0.01$; IRE vs normal liver, $P < 0.0001$; RE zones vs normal liver, $P = 0.01$). The hepatocyte apoptosis strongly correlated with PE ($r = -0.74$, $P < 0.0001$), AUT_{60} ($r = -0.63$, $P < 0.0001$), AUT_{90} ($r = -0.65$, $P < 0.0001$), AUT_{120} ($r = -0.68$, $P < 0.0001$), AUT_{150} ($r = -0.69$, $P < 0.0001$), AUT_{180} ($r = -0.71$, $P < 0.0001$), K^{trans} ($r = -0.63$, $P < 0.0001$), and v_p ($r = -0.66$, $P < 0.0001$). There was moderate correlation of hepatocyte apoptosis with TTP ($r = 0.40$, $P = 0.01$), WIS ($r = -0.54$, $P < 0.0001$), and AUT_{30} ($r = -0.60$, $P < 0.0001$). A weak correlation was observed between hepatocyte apoptosis and v_e ($r = -0.36$, $P = 0.02$).

Discussion

Our study demonstrated that TRIP-MRI not only depicts a reduction in liver tissue perfusion immediately after IRE procedures but also enables clear discrimination between IRE and RE zones immediately following IRE procedures in a rabbit liver.

Guo et al. evaluated contrast-enhanced MRI to predict the size of IRE zones in the rat liver tissues (7). The contrast agents were injected intramuscularly before IRE, and MRI examinations were performed 2 hours after IRE without dynamic phase acquisition.

Felker et al. described a three-layer histologic structure of porcine liver tissues with corresponding MRI features obtained 50 hours after IRE (10). Our study focused on the immediate response of liver tissues after IRE using not only conventional MRI to obtain the morphologic information, but also TRIP-MRI to measure the functional changes. The entire ablated regions appeared iso-intense on pre-contrast T1W and hyper-intense on T2W images. Post-contrast, heterogeneous enhancement was shown on T1W images, with a non-enhancing central core and a peripheral rim enhancement.

TRIP-MRI is a serial iterative volumetric perfusion technique and can intra-procedurally measure tissue perfusion changes (13). Previous studies compared TRIP-MRI with the conventional intra-venous contrast perfusion MRI in a rabbit VX2 liver tumor model and showed that TRIP-MRI at a 60% reduction in contrast agent dose identified more liver tumors than the IV contrast perfusion MRI. In our study, 5% gadopentetate dimeglumine was used for TRIP-MRI compared with 100% agent for intravenous contrast perfusion MRI (19, 20). In our study, the TICs showed that the wash-in and wash-out time was relatively short, which was consistent with the previous studies (19, 20). Our study also showed that PE and AUT over more than 60 s after enhancement initiation were significantly decreased from the normal liver parenchyma to RE-zones and from RE zones to IRE zones; these changes strongly correlated with histologic results. As for the quantitative parameters, K^{trans} was highest in the normal liver parenchyma, followed by RE and IRE zones. v_e in RE zones was significantly higher than in IRE zones or the normal liver parenchyma, likely due to the presence of interstitial edema and congestion in RE zones. However, there was only a weak correlation between v_e and hepatocyte apoptosis. Among the quantitative parameters, K^{trans} had a good diagnostic performance in differentiating RE from IRE zones with 85% accuracy, 77% sensitivity, and 92% specificity. It's worth noting that, AUT_{150} and AUT_{180} had the greatest ability among all the TRIP-MRI parameters to differentiate RE from IRE zones with 96% accuracy, 100% sensitivity, and 92% specificity. Our results demonstrated that semi-quantitative parameter AUT_{150} or AUT_{180} could be a potential imaging biomarker to differentiate RE from IRE zones, and easy-to-implement in clinical practice as they can be calculated without using advanced pharmacokinetic modeling. Our findings will provide fundamental preclinical validation for clinical translation.

The main limitation of our study is that TRIP-MRI was only performed at an immediate time point after IRE, and future studies will investigate delayed findings of TRIP-MRI and corresponding histologic changes after IRE to more comprehensively evaluate TRIP-MRI for differentiation of ablation zones after IRE.

In conclusion, TRIP-MRI permits to differentiate RE from IRE zones immediately after IRE procedure in the rabbit liver.

Funding:

Abbreviations:

TRIP	transcatheter intraarterial perfusion
IRE	irreversible electroporation
RE	reversible electroporation
TUNEL	transferase dUTP nick end labeling
TIC	time-intensity curve
PE	peak enhancement
TTP	time to peak
WIS	wash-in slope
AUT	area under the time-intensity curve

References

1. Facciorusso A, Serviddio G, Muscatiello N. Local ablative treatments for hepatocellular carcinoma: An updated review. World journal of gastrointestinal pharmacology and therapeutics. 2016; 7(4):477. [PubMed: 27867681]

2. Seror O. Ablative therapies: Advantages and disadvantages of radiofrequency, cryotherapy, microwave and electroporation methods, or how to choose the right method for an individual patient? Diagn Interv Imaging. 2015; 96(6):617–24. [PubMed: 25981214]

3. Narayanan G. Irreversible Electroporation. Seminars in interventional radiology. 2015; 32(4):349–55. [PubMed: 26622097]

4. Bulvik BE, Rozenblum N, Gourevich S, et al. Irreversible Electroporation versus Radiofrequency Ablation: A Comparison of Local and Systemic Effects in a Small-Animal Model. Radiology. 2016; 280(2):413–24. [PubMed: 27429143]

5. Distelmaier M, Barabasch A, Heil P, et al. Midterm Safety and Efficacy of Irreversible Electroporation of Malignant Liver Tumors Located Close to Major Portal or Hepatic Veins. Radiology. 2017; 285(3):1023–31. [PubMed: 28799842]

6. Sutter O, Calvo J, N'Kontchou G, et al. Safety and Efficacy of Irreversible Electroporation for the Treatment of Hepatocellular Carcinoma Not Amenable to Thermal Ablation Techniques: A Retrospective Single-Center Case Series. Radiology. 2017; 284(3):877–86. [PubMed: 28453431]

7. Guo Y, Zhang Y, Nijm GM, et al. Irreversible electroporation in the liver: contrast-enhanced inversion-recovery MR imaging approaches to differentiate reversibly electroporated penumbra from irreversibly electroporated ablation zones. Radiology. 2011; 258(2):461–8. [PubMed: 21131581]

8. Chung DJ, Sung K, Osuagwu FC, Wu HH, Lassman C, Lu DS. Contrast Enhancement Patterns after Irreversible Electroporation: Experimental Study of CT Perfusion Correlated to Histopathology in Normal Porcine Liver. Journal of vascular and interventional radiology : JVIR. 2016; 27(1):104–11. [PubMed: 26547121]

9. Long G, Bakos G, Shires PK, et al. Histological and finite element analysis of cell death due to irreversible electroporation. Technology in cancer research & treatment. 2014; 13(6):561–9. [PubMed: 24000980]

10. Felker ER, Dregely I, Chung DJ, et al. Irreversible Electroporation: Defining the MRI Appearance of the Ablation Zone With Histopathologic Correlation in a Porcine Liver Model. AJR American journal of roentgenology. 2017; 208(5):1141–6. [PubMed: 28177652]

11. Padia SA, Johnson GE, Yeung RS, Park JO, Hippe DS, Kogut MJ. Irreversible Electroporation in Patients with Hepatocellular Carcinoma: Immediate versus Delayed Findings at MR Imaging. Radiology. 2016; 278(1):285–94. [PubMed: 26523493]

12. Gaba RC, Jin B, Wang D, et al. Locoregional chemoembolic delivery: prediction with transcatheter intraarterial perfusion MRI. AJR Am J Roentgenol. 2012; 198(5):1196–202. [PubMed: 22528913]

13. Wang D, Jin B, Lewandowski RJ, et al. Quantitative 4D transcatheter intraarterial perfusion MRI for monitoring chemoembolization of hepatocellular carcinoma. Journal of magnetic resonance imaging : JMRI. 2010; 31(5):1106–16. [PubMed: 20432345]

14. Wang D, Gaba RC, Jin B, et al. Perfusion reduction at transcatheter intraarterial perfusion MR imaging: a promising intraprocedural biomarker to predict transplant-free survival during chemoembolization of hepatocellular carcinoma. Radiology. 2014; 272(2):587–97. [PubMed: 24678859]

15. Zhang Y, White SB, Nicolai JR, et al. Multimodality imaging to assess immediate response to irreversible electroporation in a rat liver tumor model. Radiology. 2014; 271(3):721–9. [PubMed: 24555632]

16. Zhou L, Chen TW, Zhang XM, et al. Liver dynamic contrast-enhanced MRI for staging liver fibrosis in a piglet model. J Magn Reson Imaging. 2014; 39(4):872–8. [PubMed: 24123400]

17. Tofts PS. Modeling tracer kinetics in dynamic Gd-DTPA MR imaging. Journal of magnetic resonance imaging : JMRI. 1997; 7(1):91–101. [PubMed: 9039598]

18. Tofts PS, Brix G, Buckley DL, et al. Estimating kinetic parameters from dynamic contrast-enhanced T(1)-weighted MRI of a diffusable tracer: standardized quantities and symbols. J Magn Reson Imaging. 1999; 10(3):223–32. [PubMed: 10508281]

19. Larson AC, Rhee TK, Deng J, et al. Comparison between intravenous and intraarterial contrast injections for dynamic 3D MRI of liver tumors in the VX2 rabbit model. Journal of magnetic resonance imaging : JMRI. 2006; 24(1):242–7. [PubMed: 16758469]

20. Sato KT, Wang D, Lewandowski RJ, et al. Four-dimensional transcatheter intraarterial perfusion MRI monitoring of radiofrequency ablation of rabbit VX2 liver tumors. J Magn Reson Imaging. 2011; 34(3):563–9. [PubMed: 21761464]
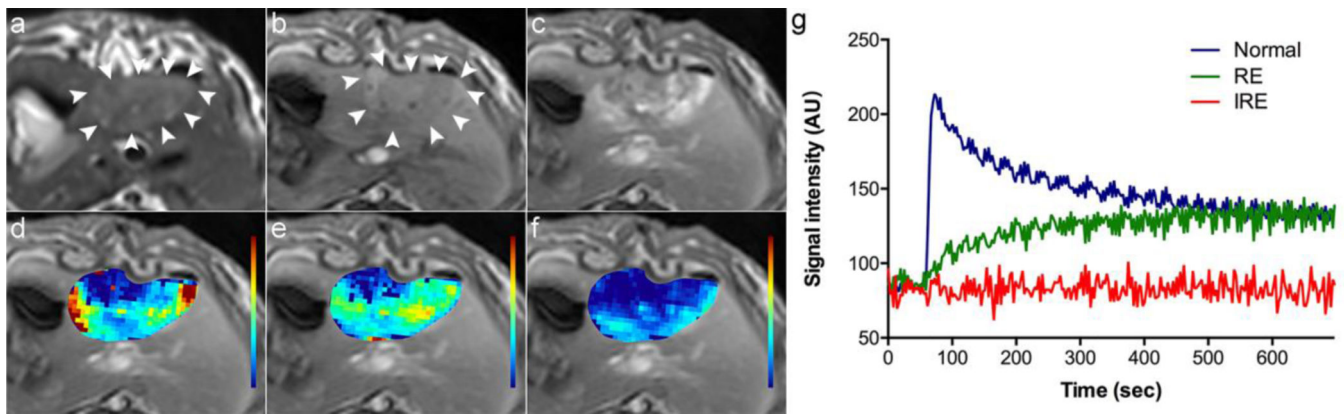
Figure 1:

Representative MRI images of the liver and corresponding time-intensity curves immediately after IRE in a single rabbit. The entire ablated zone shows hyper-intensity on the T2W image (a, arrowheads), slight hypo-intensity on the pre-contrast T1W image (b, arrowheads), and heterogeneous enhancement with a non-enhancement center and an obvious peripheral enhancement on the post-contrast T1W image (c). The maps of K^{trans} (d), v_e (e) and v_p (f) overlapped on the post-contrast T1W image clearly depicted heterogeneous perfusion of the entire ablated zone. The time-intensity curves (g) derived from the normal liver parenchyma, the RE and IRE zone show a unique pattern for each zone.
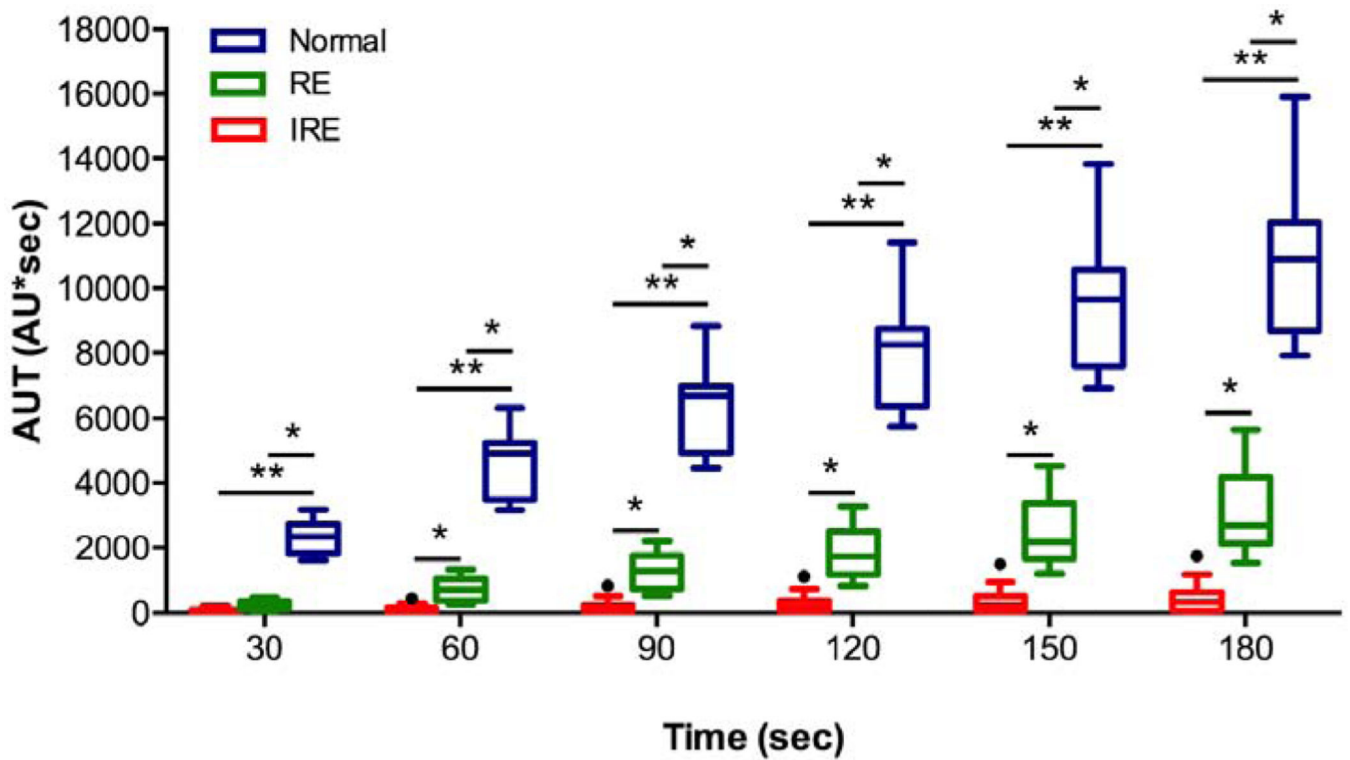
Figure 2:

The Tukey boxplot shows the areas under the time-intensity curves (AUT) over 30, 60, 90, 120, 150 and 180 seconds after the initiation of enhancement for the IRE (red, n = 13), RE zones (green, n = 13) and the normal liver parenchyma (blue, n = 13). AUT_{60}, AUT_{90}, AUT_{120}, AUT_{150}, and AUT_{180} had the ability to differentiate RE from IRE zones. The box plot displays the full range of variation (from min to max), and the dots indicate discrete values. Statistically significant differences are marked by stars (* $P < 0.05$, ** $P < 0.0001$).
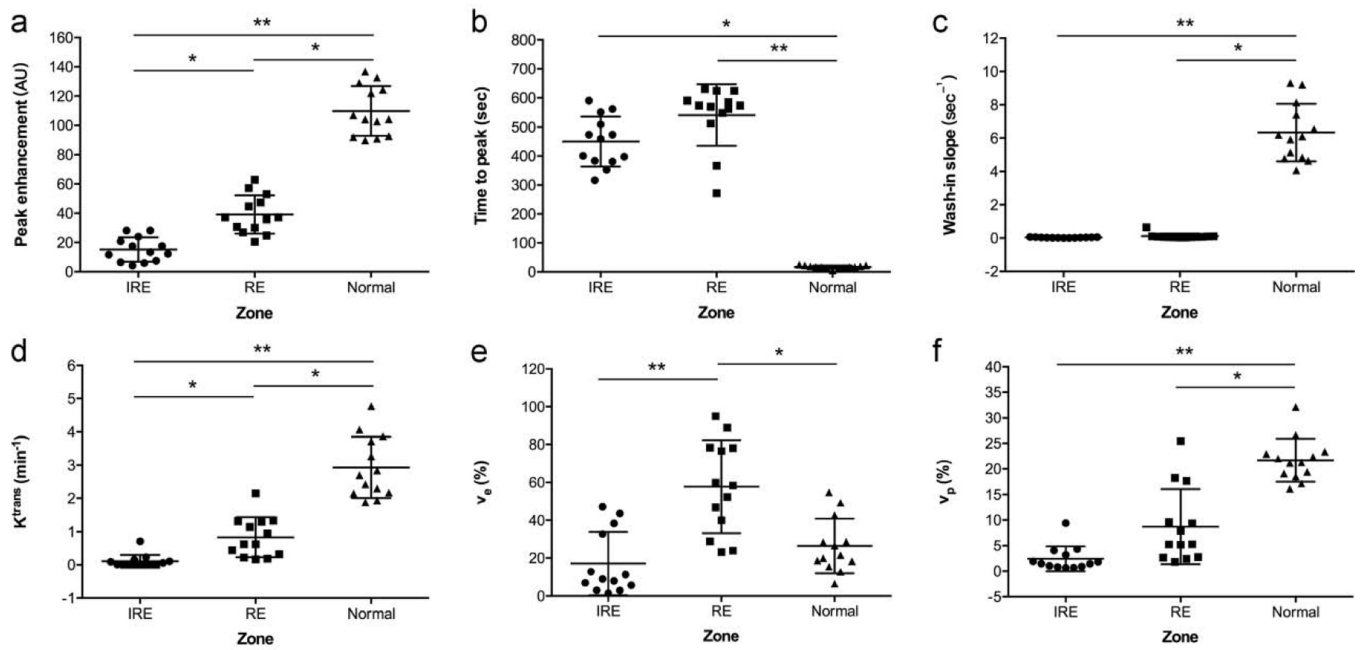
Figure 3:
Scatter dot plots show peak enhancement **(a)**, time to peak **(b)**, wash-in slope **(c)**, K^{trans} **(d)**, v_e **(e)** and v_p **(f)** for the IRE zones (n = 13), RE zones (n = 13) and the normal liver parenchyma (n = 13). Peak enhancement, K^{trans} and v_e had the ability to differentiate RE from IRE zones. Statistically significant differences are marked by stars (* $P < 0.05$, ** $P < 0.0001$). The larger horizontal bar indicates the mean value, error bars indicate standard deviations, and dots indicate individual values.
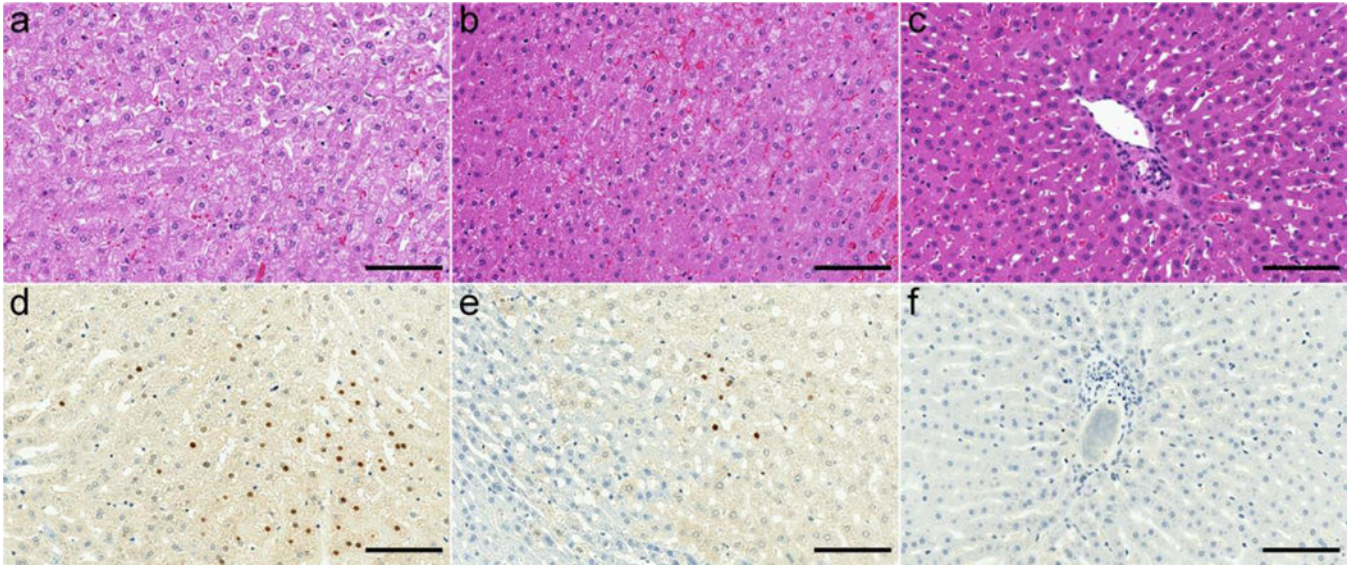
Figure 4:
Representative histologic images of the IRE zone **(a, d)**, the RE zone **(b, e)** and the normal liver parenchyma **(c, f)**. In the IRE zone, there is obvious hepatocyte necrosis and hemorrhage on the HE-stained image **(a)**, and apoptotic cells (brown stain) were about 22.7% of the total cells on the TUNEL-stained image **(d)**. In the RE zone, there is hepatocyte swelling with vacuoles, occasional hepatocyte necrosis and congestion on the HE-stained image **(b)**, and apoptotic cells (brown stain) were about 3% of the total cells on the TUNEL-stained image **(e)**. In the normal liver parenchyma, there is no obvious abnormal feature on the HE-stained image **(c)**, and no apoptosis is visible on the TUNEL-stained image **(f)**. Scale bar, 100 μm for all the images.

Table 1.

Sequences and parameters of conventional T1W, T2W, and TRIP MRI

Parameters	T2W (TSE)	T1W (FLASH)	T2W (TSE)	TRIP MRI (GRE)
Orientation	Coronal	Axial	Axial	Axial
Trigger	Respiration	None	Respiration	None
TR/TE (ms)	1769-4341/39	200/2.93	2247-4384/39	2.60/1.2
FOV (mm^2)	180×180	180×180	180×180	128×112
Matrix	192×192	224×224	192×192	128×112
Number of slices	17	17	17	20
Slice thickness/gap (mm)	2/0.6	2/0.6	2/0.6	2/0.6
Flip angle (degrees)	150	70	150	8
Bandwidth (Hz/pixel)	221	350	221	980

Note: TRIP = transcatheter intra-arterial perfusion, TSE = turbo spin echo, FLASH = fast low angle shot, GRE = gradient echo, TR = repetition time, TE = echo time, FOV = field of view.

Table 2.

Comparison of TRIP MRI parameters among IRE, RE zones and normal liver parenchyma

Parameters	IRE Zone	RE Zone	Normal Liver	*P* Value[*]		
				IRE vs RE	IRE vs Normal	RE vs Normal
PE	15 ± 8	39 ± 13	110 ± 17	0.025	< 0.0001	0.007
TTP	450 ± 86	541 ± 106	17 ± 5	0.29	0.001	< 0.0001
WIS	0.04 ± 0.02	0.2 ± 0.2	6.3 ± 1.7	0.07	< 0.0001	0.004
AUT_{30}	58 ± 67	231 ± 145	2381 ± 532	0.06	< 0.0001	0.004
AUT_{60}	116 ± 126	702 ± 354	4637 ± 1065	0.02	< 0.0001	0.008
AUT_{90}	193 ± 237	1226 ± 564	6344 ± 1428	0.017	< 0.0001	0.009
AUT_{120}	281 ± 319	1843 ± 791	8049 ± 1772	0.014	< 0.0001	0.01
AUT_{150}	376 ± 421	2535 ± 1054	9616 ± 2163	0.012	< 0.0001	0.01
AUT_{180}	460 ± 500	3193 ± 1307	10962 ± 2484	0.012	< 0.0001	0.01
K^{trans}	0.1 ± 0.2	0.8 ± 0.6	2.9 ± 0.9	0.027	< 0.0001	0.009
v_e	17 ± 17	58 ± 25	26 ± 14	< 0.0001	0.67	0.001
v_p	2.4 ± 2.4	8.7 ± 7.4	22 ± 4	0.05	< 0.0001	0.016

Note: Data was represented as mean ± SD. PE = peak enhancement, TTP = time to peak, WIS = wash-in slope, AUT = area under the time-intensity curve.

[*] $P < 0.05$ was considered to indicate a significant difference.

Table 3.

ROC Curve Analysis of TRIP MRI Parameters in Differentiating RE from IRE Zones

Parameters	AUC[*]	Cut-off Value	Accuracy (%)[†]	Sensitivity (%)[†]	Specificity (%)[†]	PPV (%)[†]	NPV (%)[†]
PE	0.95 (0.88,1.00)	24.4	88.5 (23/26)	92.3 (12/13)	84.6 (11/13)	85.7 (12/14)	91.7 (11/12)
AUT_{60}	0.96 (0.90,1.00)	308.9	88.5 (23/26)	84.6 (11/13)	92.3 (12/13)	91.7 (11/12)	85.7 (12/14)
AUT_{90}	0.98 (0.92,1.00)	520.5	96.2 (25/26)	100 (13/13)	92.3 (12/13)	92.9 (13/14)	100 (12/12)
AUT_{120}	0.99 (0.96,1.00)	783.8	96.2 (25/26)	100 (13/13)	92.3 (12/13)	92.9 (13/14)	100 (12/12)
AUT_{150}	0.99 (0.98,1.00)	1066	96.2 (25/26)	100 (13/13)	92.3 (12/13)	92.9 (13/14)	100 (12/12)
AUT_{180}	0.99 (0.98,1.00)	1343	96.2 (25/26)	100 (13/13)	92.3 (12/13)	92.9 (13/14)	100 (12/12)
K^{trans}	0.94 (0.85,1.00)	0.28	84.6 (22/26)	76.9 (10/13)	92.3 (12/13)	90.9 (10/11)	80 (12/15)
V_e	0.91 (0.80,1.00)	45.2	80.8 (21/26)	69.2 (9/13)	92.3 (12/13)	90 (9/10)	75 (12/16)

Note:

[*] Data in parentheses are 95% confidence interval.

[†] Data in parentheses are raw data. PE = peak enhancement, AUC = area under the ROC curve, PPV = positive predictive value, NPV = negative predictive value, AUT = area under the time-intensity curve.